ROYAL SOCIETY
OF CHEMISTRY

PAPER

Check for updates

Research on the initial corrosion behavior of A100 steel in salt fog-SO$_2$ environment

Yong Zhang,*[a] Hanyao Xiao, [ID][a] Wenfei Yang,*[a] Weijie Fan,[a] Andong Wang,[a] Jia Li [ID][b] and Hongjun Zhao[c]

To investigate the service performance of A100 steel with the chemical composition 23Co$_{14}$Ni$_{12}$Cr$_3$Mo in actual ship deck environments, this study innovatively adopts the ASTM G85 "salt spray-SO$_2$ modified salt spray test" to simulate the weakly acidic marine atmosphere containing engine exhaust pollutants. This approach addresses the limitation of domestic studies that primarily rely on neutral salt spray tests following GJB150.11A, which fail to reflect complex service conditions. The corrosion behavior, product composition and electrochemical kinetics of A100 steel were systematically characterized using multiple techniques including SEM, XRD, XPS, FT-IR, EDS, electrochemical workstation and EBSD. Results show that the corrosion process exhibits triphasic kinetics: rapid initial corrosion from 2 to 4 days due to direct contact between the metal and corrosive medium, with charge transfer resistance (R_{ct}) decreasing from 2860 Ω cm^2 to 1029 Ω cm^2 and corrosion current density (I_{corr}) increasing from 5.09 μA cm^{-2} to 7.35 μA cm^{-2}; decelerated degradation from 4 to 8 days by the formation of a dual-layer rust structure consisting of a dense inner layer of Fe$_3$O$_4$ and γ-FeOOH as well as a porous outer layer of Fe$_2$O$_3$, with R_{ct} peaking at 5421 Ω cm^2 and I_{corr} dropping to the minimum of 1.73 μA cm^{-2}; and renewed acceleration from 8 to 10 days caused by the synergistic damage of Cl$^-$ and HSO$_3^-$ to the rust layer, with R_{ct} plummeting to 426 Ω cm^2 and I_{corr} surging to 23.44 μA cm^{-2}. Alloying elements including Cr, Co and Ni regulate corrosion resistance by modifying the rust layer structure and electrochemical properties. Microstructurally, the initial passivation of austenite delays corrosion, while the subsequent dissolution of martensite and the establishment of a dynamic phase equilibrium ultimately expose austenite, accelerating degradation beyond 10 days. This work clarifies the corrosion mechanism of A100 steel under salt spray-SO$_2$ coupling, providing a reliable experimental basis and theoretical support for its safe application in marine aviation equipment.

1 Introduction

In recent years, with the transformation and upgrading of China's maritime strategy, there has been increasing attention on the survival and adaptability of aircraft in marine environments.[1] Aircraft that remain on decks or in ship hangars for extended periods are subjected to the corrosive effects of the marine atmosphere. The harsh marine atmospheric environment not only affects aircraft performance but also imposes higher demands on maintenance and upkeep. The new high-strength A100 steel (23Co$_{14}$Ni$_{12}$Cr$_3$Mo), known for its excellent toughness, stress-fatigue resistance, and corrosion resistance,[2] has been widely used in marine aviation equipment, particularly in landing gear structures.[3] However, the high-

temperature, high-humidity, and high-salinity characteristic of marine atmospheres make aircraft structures particularly vulnerable to corrosion degradation.[4] Research on the corrosion behavior of A100 steel in complex atmospheric environments is of significant importance for the safe operation of aircraft in harsh marine conditions. Currently, both domestic and international research on the corrosion of high-strength steels primarily focuses on corrosion-induced mechanical issues, and China's research in this area is generally aligned with global trends.[5,6] With the deepening of research on marine environments, conventional neutral salt spray tests (NSS) and GJB150.11A standards have proven insufficient for effectively assessing the corrosion resistance of materials in marine conditions, as they cannot simulate the weakly acidic environment and Cl$^-$–HSO$_3^-$ synergistic corrosion induced by SO$_2$ in engine exhaust. In contrast, ASTM G85 can accurately replicate the pollutant composition and dynamic corrosion cycles of actual ship decks, making it more suitable for revealing the service-related corrosion behavior of A100 steel.

[a] Naval Aviation University Department of Aviation Mechanics, Qingdao, 266041, PR China. E-mail: zhangyong308@126.com; yangwf_dlut@163.com

[b] State Key Laboratory of Advanced Design and Manufacturing Technology for Vehicle, College of Mechanical and Vehicle Engineering, Hunan University, Changsha, 410082, PR China

[c] Naval Aviation University, Yantai, 264000, PR China

Huang Tao[7] conducted preliminary research on the rust characteristics and corrosion resistance of high-strength steel in neutral salt solutions. It was found that a dense inner rust layer can effectively prevent the penetration of Cl^-, thereby enhancing the material's corrosion resistance.[8] Based on Huang Tao's neutral salt spray experiments, Guo Mingxiao and colleagues investigated the corrosion mechanism of SO_2 under acidic salt spray conditions.[9,10] The study revealed that the synergistic effect of SO_2 and Cl^- promoted corrosion in the early stages of the experiment, while the SO_2/Cl^- ratio did not alter the composition of the corrosion products on the carbon steel surface. Additionally, SO_2 facilitated the homogenization of carbon steel corrosion. Qian Ang et al.[11,12] studied the corrosion and electrochemical characteristics of A100 steel in neutral salt spray environments. Their research indicated that the surface corrosion product layer effectively hindered the penetration and diffusion of the corrosive solution into the substrate, delaying the corrosion process and providing good protection to the substrate. Yang Wendi and Zhao Lianhong[13] utilized laser cladding technology to prepare a CoCrNiNb0.1 + xB4C high-entropy alloy coatings on the surface of A100 steel. The results demonstrated that the addition of B4C led to an increase in the coating's microhardness but a reduction in its corrosion resistance. Vishwajeet Bachhar's team demonstrated that Solanum chrysotrichum extract, rich in bioactive phytochemicals, achieves a maximum corrosion inhibition efficiency of 93.38% for mild steel (MS) in 1.0 M HCl at 1.20 g L^{-1} concentration (following Langmuir isotherm) while exhibiting antioxidant and antibacterial properties, as evidenced by multifaceted characterization and computational analyses.[14,15] With the deepening of research on marine environments, conventional neutral salt spray tests and evaluation metrics have proven insufficient for effectively assessing the corrosion resistance of materials in marine conditions, as they significantly differ from the complex deck environments. The deck surface is exposed to a large amount of exhaust fumes emitted by engines during operation, containing gases such as NO_2 and SO_2, with SO_2 posing the greatest threat to the corrosion damage of aircraft structures.[16] Currently, domestic studies on the corrosion behavior of A100 steel primarily rely on neutral salt spray tests, conducted in accordance with GJB150.11A "Laboratory Environmental Test Methods for Military Equipment: Salt Spray Test" for relevant testing and verification.[17] Compared to neutral salt spray environments, the weakly acidic environment resulting from the combined effects of salt spray and SO_2 more closely resembles the actual conditions on ship decks. The U.S. military has extensively applied the "salt spray-SO_2" testing method to evaluate the adaptability of materials in marine deck environments, and after decades of development and application, this method has matured.[18] The U.S. Department of Defense's "Environmental Engineering Considerations and Laboratory Tests" includes ASTM.G85 "Modified Salt Spray Test Methods, "with the "salt spray-SO_2" testing procedure incorporated into the environmental test method standards MIL-STD-810 versions F and G. The provided data indicate that corrosion exposure tests on ships align with the results of ASTM.G85 "salt spray-SO_2" tests.[19–21] Diverging from traditional

GJB150.11A methodologies, this study adopts the ASTM G85-based modified salt spray test to evaluate A100 steel specimens, aiming to better simulate the service environment of aircraft on ship decks in China. As A100 steel is a primary material for aircraft landing gear, studying it using the salt spray-SO_2 corrosion test standard holds significant reference value. This paper investigates the corrosion behavior and electrochemical characteristics of A100 steel under salt spray-SO_2 conditions, providing valuable insights for the safe service of this material in harsh deck environments.

2   Experimental

2.1   Experimental materials

The test specimens were fabricated from A100 high-strength alloy steel and machined into cylindrical geometries with dimensions of 6×6 mm (Fig. 1). Prior to corrosion testing, all specimens underwent standardized surface treatment to ensure consistent initial conditions: sequentially ground with sandpapers to remove machining defects, ultrasonically cleaned in anhydrous ethanol for 15 minutes to eliminate surface contaminants, and dried with high-purity nitrogen.The heat treatment procedures included: oil quenching at (885 ± 14)°C for 60 minutes, cryogenic treatment at (-73 ± 8) °C for 60 minutes followed by air reversion, and final tempering at (482 ± 3) °C for 6 h with air cooling. Table 1 present the chemical composition and mechanical properties, respectively. The alloy primarily consists of Fe, Co, and Ni with trace amounts of Cr, Mo, and Mn. It exhibits exceptional strength, with a tensile strength of 1970 MPa, and toughness, making it suitable for aircraft landing gear applications.

2.2   Salt Spray-SO_2 corrosion testing

According to ASTM G85, a HKT 3000 Clima salt spray-SO_2 chamber (Kohler Co.) was employed to simulate marine atmospheric conditions. The test parameters strictly corresponded to the actual environmental characteristics of ship decks to ensure simulation authenticity: the exposure zone temperature was maintained at 35 ± 1 °C, with a saturated tower temperature of 47 ± 1 °C. These parameters align with the typical marine

Fig. 1   Sample size and physical image.

Table 1   Chemical composition of A100 steel wt%

C	Co	Ni	Cr	Mo	Mn	Si	Fe
0.229	13.46	11.23	3.01	1.22	0.02	0.03	Bal

atmospheric temperature range of 28–36 °C in coastal navigation areas,[14] while accounting for localized surface temperature increases of 3–5 °C caused by engine exhaust. The saturated tower temperature maintained a relative humidity >95%, consistent with the average marine atmospheric humidity of 85–98%.[18] The selected SO_2 flow rate of 35 cm^3 (min m^{-3}) fell within the actual SO_2 concentration range of 10–50 cm^3 (min m^{-3}) on ship decks,[14] specifically simulating peak SO_2 exposure from engine exhaust during routine aircraft takeoffs and landings, where SO_2 constitutes 60–70% of acidic pollutants.[21] The 5 wt% NaCl spray solution matched the salinity of marine atmospheric aerosols (3–6 wt%) in offshore environments,[19] reflecting the high-salinity corrosion stress on deck materials. A cyclic protocol comprising 5 hours of salt spray followed by 1 hour of SO_2 injection (repeated four times daily, 6-hours cycles) was implemented to reproduce the dynamic alternation of "salt spray deposition–SO_2 emission" in practical scenarios: the 5-hours salt spray phase simulated continuous salt exposure during aircraft parking periods, while the 1-hour SO_2 injection replicated the periodic SO_2 release during daily engine startups (2–3 cycles per day) (Fig. 2).[18] This cycling pattern has been validated through U.S. Navy vessel tests, demonstrating a strong correlation (>0.9) with actual corrosion kinetics.[20] Six groups of specimens (three replicates each) were extracted at 2, 4, 6, 8, and 10 days for corrosion morphology analysis and electrochemical testing. All data presented in this study are the mean values of three parallel specimens, which helps reduce experimental errors and ensures the accuracy and reproducibility of the results.

2.3 Electrochemical characterization

Electrochemical measurements were conducted using a PAR-STAT 4000A workstation (Princeton Applied Research). Post-corrosion specimens were air-dried, welded with central copper leads, and cold-mounted prior to immersion in 5% NaCl at 25 °C. A three-electrode system was employed, consisting of

a saturated calomel reference electrode (SCE) and a platinum counter electrode. After a stabilization period of 30 minutes, electrochemical impedance spectroscopy (EIS) was performed over a frequency range from 10^5 to 10^{-2} Hz, with a 10 mV amplitude and 30 data points. Potentiodynamic polarization scans were conducted from −0.4 to 0.4 V, utilizing a 0.5 mV step size, a 3-seconds duration per step, and a scan rate of 0.166 mV s^{-1}. The data were analyzed using Zsimpwin and Cview software. Micro-regional electrochemical mapping of a 3 × 3 mm area was performed with a VersaSCAN SKP system (Princeton), employing a 100 μm step size, an 80 μm probe distance, and a 25 μm amplitude.

2.4 Macro/microstructural analysis and corrosion product characterization

Corrosion morphology was examined using an Olympus DSX500 3D microscope and Hitachi S-3400N SEM. Initial low-magnification observations documented the coloration and distribution of the rust layer.XRD analysis (Cu Kα, 40 kV/40 mA, 5–90° range, 2° per min) characterized the composition of the rust layer after 10-days exposure. XPS (Thermo Scientific ESCALAB 250Xi, Al Kα 1486.6 eV, 150 W) determined the elemental oxidation states under ultrahigh vacuum conditions ($P < 8 × 10^{-6}$ bar), with C 1s (284.8 eV) used as a reference. EDS elemental mapping and FT-IR chemical bonding analysis complemented the phase identification. EBSD (EDAX Velocity Super, 20 kV, 40 nA, 2500 pts per s) elucidated the effects of grain boundary on corrosion progression. The integration of multimodal data ensured analytical reliability.For EBSD characterization, specimens were further polished with 0.05 μm colloidal silica after the initial mirror-finish treatment to eliminate surface stress and oxide films, then ultrasonically cleaned in anhydrous ethanol for 10 minutes and dried with high-purity nitrogen; EBSD tests were performed using an EDAX Velocity Super system with a scanning area of 3 × 3 mm per specimen, a step size of 0.5 μm, and operating parameters of 20 kV, 40 nA, 2500 pts per s, to elucidate the effects of grain boundary on corrosion progression. The integration of multimodal data ensured analytical reliability.

3 Result and analysis

3.1 Corrosion morphology and product analysis

Fig. 3 illustrates the macroscopic surface evolution of A100 steel during salt spray-SO_2 testing. After 2-days exposure, numerous dense corrosion pits appear, accompanied by dark brown discoloration and localized reddish-brown corrosion products, along with a loss of metallic luster. On the 4th day, these products develop into patchy rust deposits characterized by powdery detachment, while the dimensions of the pits increase, indicating the formation of iron oxide. Specimens examined the 6th day display extensive reddish-brown outer rust layers overlaying darker inner corrosion products. On the 8th day, a distinct dual-layer rust structure emerges: a reddish-brown outer layer (likely $FeOOH/Fe(OH)_3$) and a compact black inner layer (presumed Fe_3O_4),[22] with surface-deposited NaCl crystals
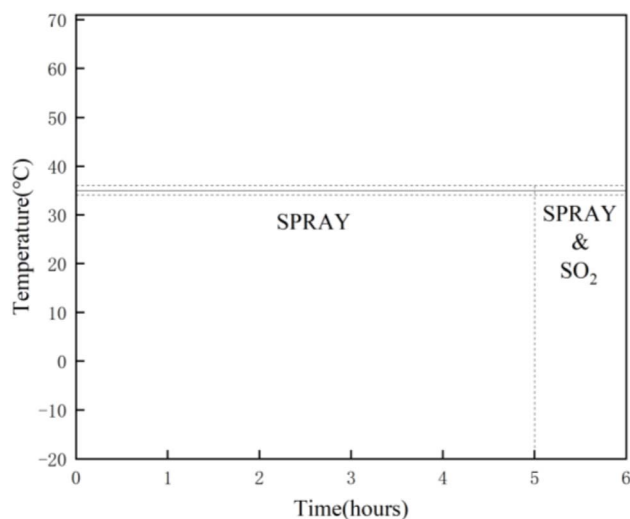
Fig. 2 Salt spray-SO_2 test scheme.

identified *via* SEM (Fig. 3e). Prolonged exposure until the 10th day results in the formation of lamellar yellow surface layers, indicative of sulfur-containing compounds. Progressive corrosion expansion is evident as color transitions from reddish-brown to yellowish hues across increasingly affected areas. The comparative analysis with neutral salt spray
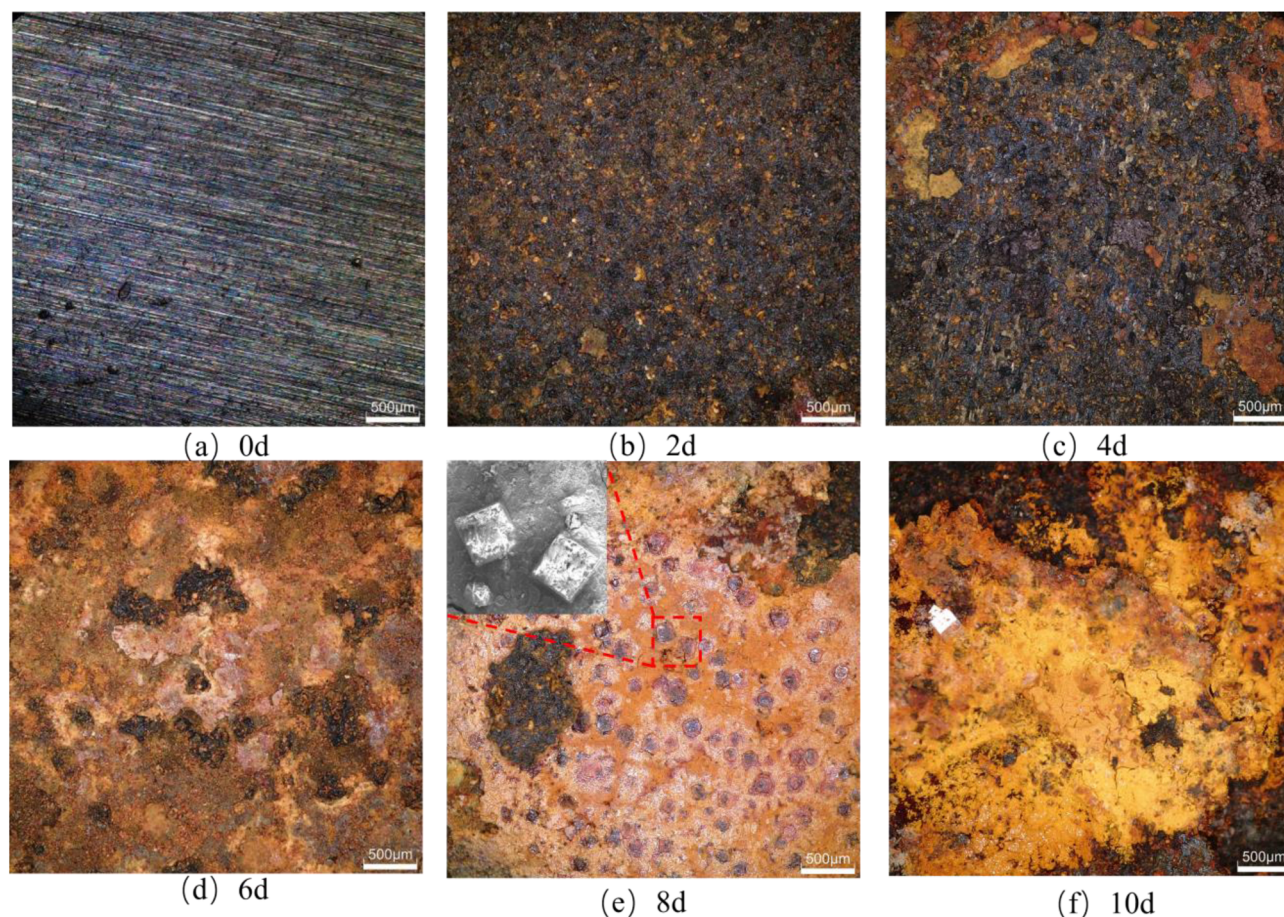

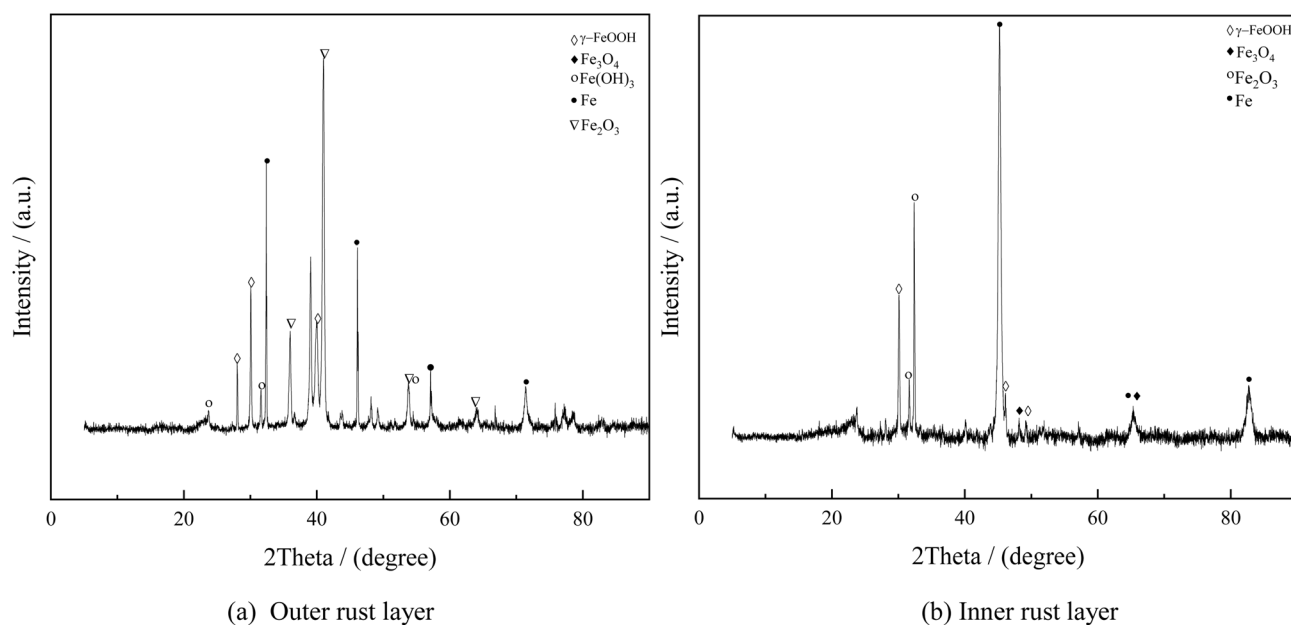Fig. 3 Corrosion morphology of salt spray–SO$_2$ after different time.

Fig. 4 Analysis results of internal and external rust layer of XRD after salt spray–SO$_2$ corrosion for 10 days.

environments[2,23] confirms accelerated degradation under combined salt spray-SO_2 conditions, as evidenced by enhanced surface deterioration at equivalent exposure durations.

Furthermore, A100 steel also contains small amounts of metallic elements such as Co, Ni, and Cr, which influence the formation of corrosion products to some extent:[24] Cr in A100
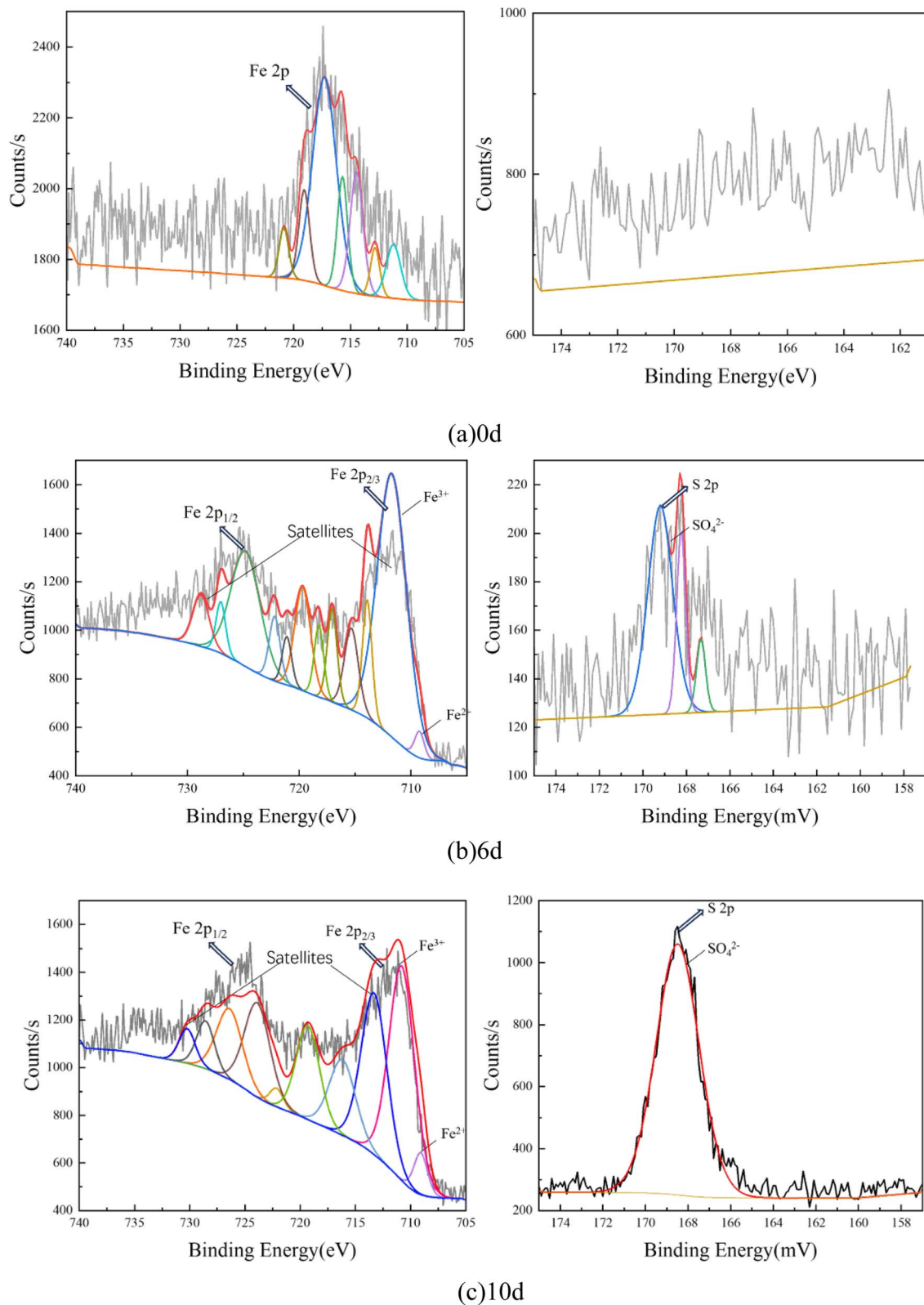

Fig. 5 Fe 2p and S 2p spectra after 10 days of corrosion.

steel imparts cation selectivity to γ-FeOOH, preventing the ingress of Cl^-; Co can exist in small amounts as CoOOH within FeOOH, increasing the electrochemical impedance of the corrosion product layer; Ni allows the Ecorr of A100 steel to shift in the positive direction, refines the grains of the internal corrosion products, increases their density, promoting the generation of the inner rust layer. These elements collectively improve the initial protective performance of corrosion products, but their regulatory effect on rust layer compactness gradually weakens with the corrosion process under the synergistic erosion of Cl^- and HSO_3^-.

Fig. 4 presents XRD analysis results of the outer and inner rust layers on A100 steel after 10 days of corrosion. The corrosion products of high-strength steel typically exhibit a dual-layer structure: a loosely adherent outer rust layer and a compact inner layer directly adjacent to the substrate. Following the natural air-drying of corroded specimens, XRD scanning of the upper surface revealed the composition of the outer layer (Fig. 4a). The subsequent removal of superficial rust through ethanol wiping exposed the dense inner layer for characterization (Fig. 4b). A comparative analysis with XRD standard patterns and existing literature[2] identified the outer layer as primarily containing Fe_2O_3, γ-FeOOH, and $Fe(OH)_3$, while the inner layer consisted predominantly of Fe_3O_4 and γ-FeOOH. These phases correspond to distinct physical properties: the outer layer manifested as a porous reddish-brown substance, contrasting with the compact black morphology of the inner layer.

Fig. 5a–c presents XPS spectra of corroded surfaces at varying exposure durations. Reference standards indicate that at 0 days, the Fe 2p spectrum displays unresolved valence states,

indicating a predominant metallic iron, while the S 2p spectrum exhibits noisy signals with negligible sulfur content. After 6 and 10 days of corrosion, characteristic Fe $2p_{1/2}$ and Fe $2p_{3/2}$ peaks appear at 725 eV and 711 eV, respectively. The Fe 2p peaks exhibit corresponding satellite features at higher binding energies – 731.8 eV and 717.7 eV for Fe^{3+}. Peak deconvolution reveals distinct binding energies of 710.8 eV (Fe^{3+}) and 709.6 eV (Fe^{2+}), confirming their coexistence. Quantitative analysis *via* peak area integration yields the Fe^{2+}/Fe^{3+} molar ratios: 0.32 ± 0.04 (6 days) and 0.21 ± 0.03 (10 days), indicating an increasing dominance of Fe^{3+} with prolonged corrosion. This trend aligns with the redox instability of Fe^{2+}, which is readily oxidized to Fe^{3+} under the weakly acidic salt spray-SO_2 environment,[25] and correlates with the formation of sulfur-containing corrosion products. The predominance of Fe^{3+} is consistent with XRD results, which align with the redox instability of Fe^{2+} and its tendency to oxidize to Fe^{3+}.[25] Fig. 5c displays the S 2p spectrum, featuring a prominent single peak at 169 eV, which corresponds to the SO_4^{2-} reference in the Avantage database. Combined with Fe 2p analysis, this confirms the formation of sulfate through Fe^{3+}–SO_4^{2-} coordination in corrosion products.[26]

Fig. 6 presents SEM observations of specimen surfaces at 0, 6, and 10 days of corrosion exposure (all subfigures with a scale bar of 50.0 μm). The progressive densification of corrosion products is evident, with complete substrate coverage by porous rust layers containing microcracks observed at 6 days (Fig. 6b). This is followed by a reduction in crack dimensions and enhanced in layer compactness at 10 days (Fig. 6c). EDS elemental mapping across three representative regions (Tables 2–4) reveals an increase in sulfur content with prolonged exposure, confirming the incorporation of sulfur compounds.
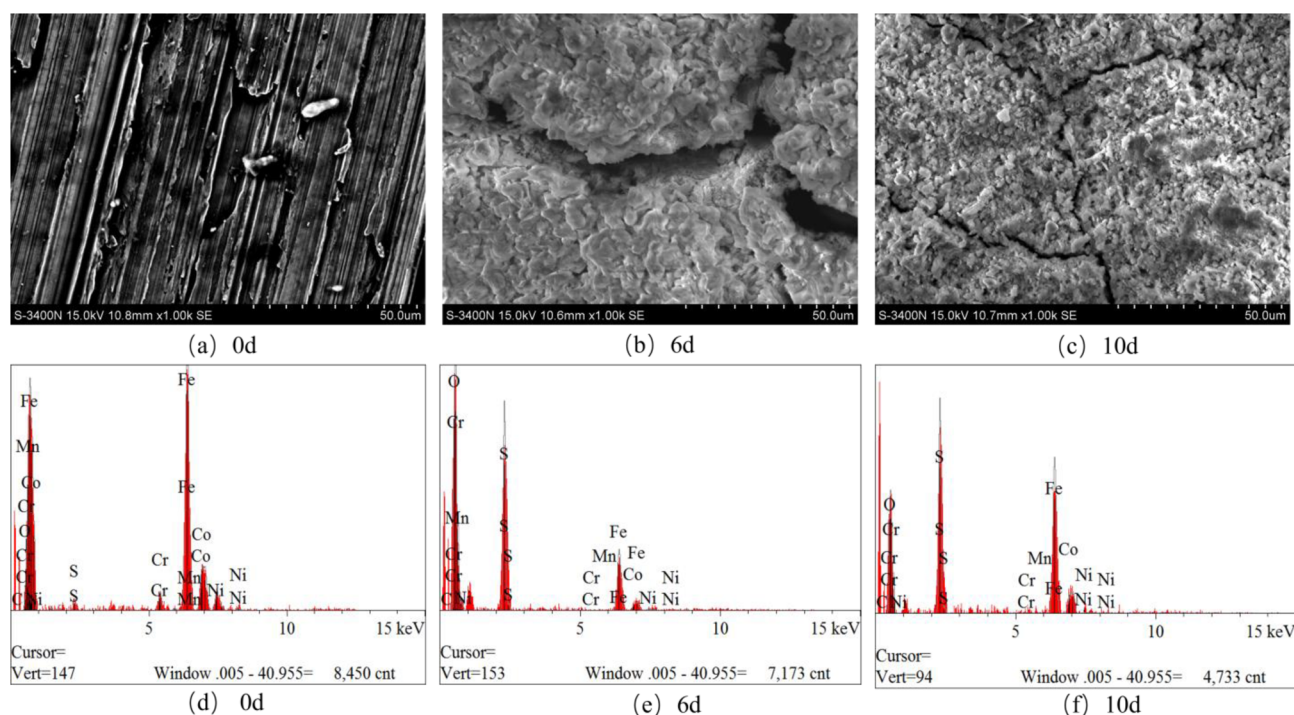

Fig. 6 SEM images and EDS analysis of different corrosion cycles.

Cross-sectional analysis demonstrates a dominance of iron and oxygen in both rust layers, which can be attributed to redox reactions occurring under salt spray-SO$_2$ conditions. The cathodic oxygen reduction facilitates anodic dissolution of iron, resulting in the formation of Fe$_2$O$_3$ and FeOOH.[27] The corrosion mechanism involves two accelerators: chloride ions (0.362 nm diameter) penetrate surface oxides to initiate pitting corrosion,[28] while SO$_2$-derived HSO$_3^-$ acidifies the electrolyte, synergistically enhancing reaction kinetics versus neutral environments.[29] Alloying elements exert microstructure-modifying effects: chromium enables γ-FeOOH's cation-selective barrier against chloride ingress; cobalt incorporation as CoOOH increases electrochemical impedance; nickel elevates corrosion potential (E_{corr}) while refining grain structure to promote the formation of a dense inner layer.[28,30,31]

Fig. 7 presents the results of Fourier-transform infrared spectroscopy (FTIR) analysis of corrosion products under salt spray-SO$_2$ exposure. The presence of identical infrared absorption bands across various exposure periods demonstrate consistent compositional profiles, primarily containing Fe$_3$O$_4$, γ-FeOOH, and Fe$_2$(SO$_4$)$_3$.[1] Characteristic vibrational modes are observed at 605 cm^{-1} (Fe–O stretching/bending), 832 cm^{-1} (γ-

FeOOH symmetric stretching), and 998 cm^{-1} (γ-FeOOH anti-symmetric vibration). The prominence of the latter among FeOOH polymorphs suggests enhanced corrosion resistance.[1] The broad band at 3350 cm^{-1} corresponds to O–H stretching in Fe^{2+}-bound hydroxyl groups and adsorbed water molecules, whilethe feature at 1635 cm^{-1} is attributed to H–O–H bending vibrations.[32] Notably, the peak at 1096 cm^{-1} aligns with S=O/O=S=O stretching in SO$_4^{2-}$,[33] corroborating findings from EDS and XPS (Fig. 4 and 5). The spectral signature at 605 cm^{-1} further confirms Fe–O–H lattice vibrations in iron oxyhydroxide structures,[34] validating sulfate incorporation and the evolution of iron oxide phases during corrosive degradation.

3.2 Electrochemical test results and analysis

Fig. 8 presents the results of electrochemical impedance spectroscopy (EIS) analysis of A100 steel immersed in 5% NaCl solution at varying corrosion durations. The reduction in capacitive arc radii from day 2 to 4 (Fig. 8a) indicate accelerated reaction kinetics during initial exposure period. The subsequent accumulation of corrosion products between days 6 and 8 leads to the formation of protective rust layers that penetration of HSO$_3^-$/Cl$^-$ ions, as evidenced by the increasing arc radii. Bode magnitude analysis (Fig. 8b) reveals a decline in corrosion resistance from days 2 to 4, attributed to direct metal–electrolyte interaction prior to the formation of the protective layer. The progressive densification of corrosion products starting from day 6 establishes effective diffusion barriers, reaching the maximum impedance modulus by day 8. However, the degradation of the outer layer initiates a dynamic equilibrium between protective effects and renewed corrosion, resulting in a reduced modulus on day 10 compared to day 4. Characteristic phase angle maxima in the 10^0–10^2 Hz range (Fig. 8c) correspond to redox reaction time constants under weak acidic salt spray-SO$_2$ conditions,[22] consistent with modulus evolution. The dispersion effects noted in the analysis, attributed to electrode surface heterogeneity and limitations in solution conductivity, necessitate the replacement of ideal capacitors with constant phase element (CPE) components in equivalent circuit modeling.

$$Z_{CPE} = \frac{1}{A(j\omega)^k} \tag{1}$$

The equivalent circuit model utilizes the relationship $Z_{CPE} = \frac{1}{A(j\omega)^k}$, where A represents the magnitude of capacitive

Table 2 The element content on the surface of the specimen after corrosion for 0 days

Element	O	Si	S	Cr	Mn	Fe	Co	Ni
Atomic (%)	0.14	0.41	0.00	2.35	0.00	73.07	13.26	9.19
Concentration (%)	0.04	0.21	0.00	2.18	0.00	73.05	13.99	9.65

Table 3 The element content on the surface of the specimen after corrosion for 6 days

Element	O	Si	S	Cr	Mn	Fe	Co	Ni
Atomic (%)	45.46	0.20	24.79	0.00	0.03	24.67	3.41	1.30
Concentration (%)	22.81	0.18	24.93	0.00	0.05	43.21	6.30	2.40

Table 4 The element content on the surface of the specimen after corrosion for 10 days

Element	O	Si	S	Cr	Mn	Fe	Co	Ni
Atomic (%)	12.52	0.11	28.13	0.13	0.17	48.39	5.15	5.07
Concentration (%)	4.52	0.18	20.34	0.16	0.22	60.95	6.84	6.72

Table 5 Fitting results of electrochemical impedance spectroscopy

Salt spray time	R_s (Ω cm^2)	CPE$_{(dl)}$ (μF cm^{-2})	n_d	R_f (Ω cm^2)	CPE$_{(f)}$ (μF cm^{-2})	n_f	R_{ct} (Ω cm^2)	χ^2
2 days	8.11	187.2	0.862	20.16	13.03	0.855	2860	0.0032
4 days	5.97	29.46	0.569	19.63	89.26	0.756	1029	0.0041
6 days	4.77	26.59	0.827	16.96	43.19	0.850	4263	0.0028
8 days	3.56	75.21	0.715	27.21	55.27	0.826	5421	0.0025
10 days	2.14	10.81	0.892	7.56	45.62	0.762	426	0.0053
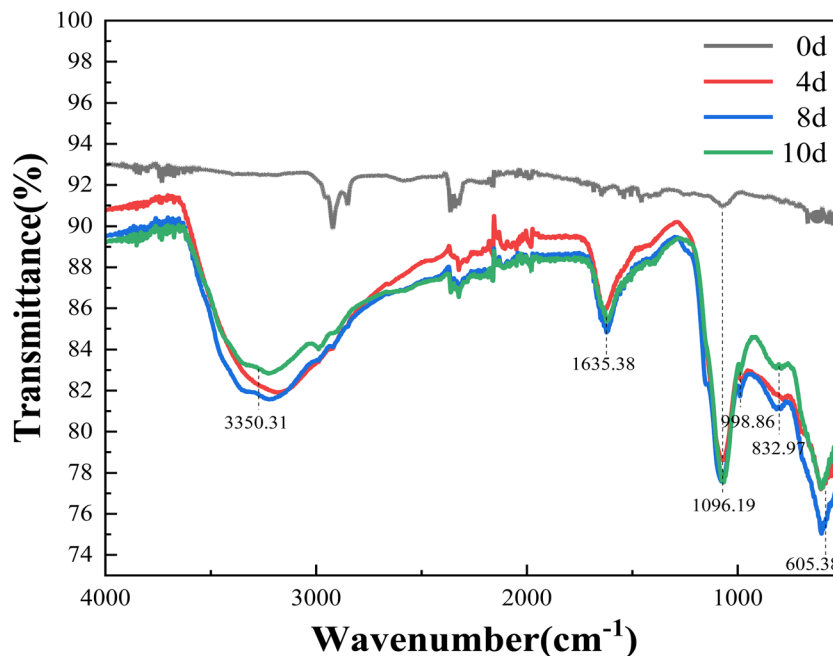
Fig. 7   FT-IR spectra of etching for different days.

(a) Nyquist plot   (b) Bode plot
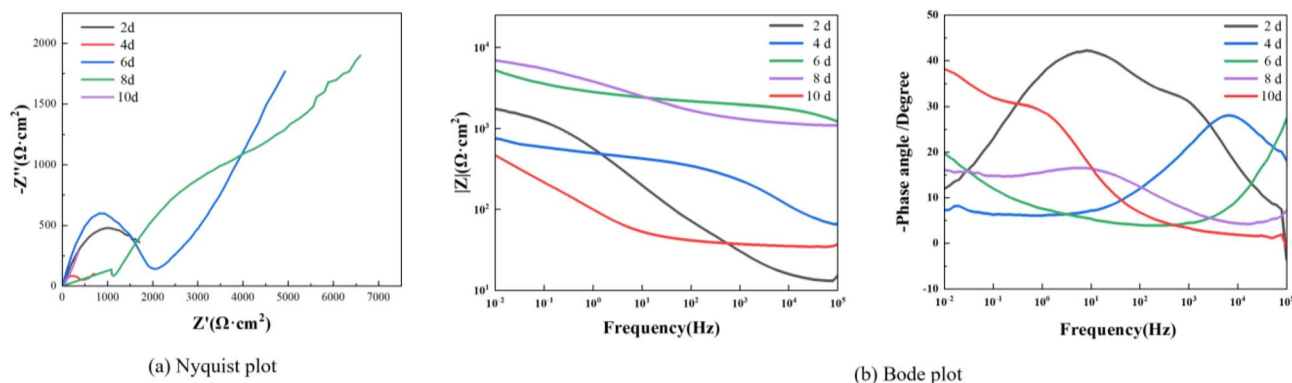
Fig. 8   Ac Impedance Diagram of A100 Steel in 5% NaCl solution under different corrosion time.

reactance/admittance, j denotes the imaginary unit, ω is the angular frequency, and k signifies the dispersion coefficient. In the context of the rust layer on A100 steel, a five-element equivalent circuit with film components (shown in Fig. 8) was selected to fit the electrochemical impedance spectroscopy data, with detailed parameters provided in Table 5. The circuit components include: R_s (NaCl solution resistance), R_{ct} (charge transfer resistance), CPE$_{dl}$ (comprising double-layer capacitance C_d and dispersion index n_d), CPE$_f$ (containing film capacitance C_f and dispersion index n_f), and R_f (passive film resistance).R_f reflects the structural characteristics of passive films, while R_{ct} corresponds to the resistance encountered during charge transfer through the electrical double layer at the substrate–electrolyte interface. Higher R_{ct} values indicate denser corrosion product layers that prevent corrosive media penetration, thereby enhancing corrosion resistance.

Conversely, lower R_{ct} suggests porous rust layers that facilitate charge transfer and accelerate material degradation.[35,36]

Based on the corrosion characteristics of A100 steel and electrochemical impedance spectroscopy (EIS) features, the five-element equivalent circuit is selected (Fig. 9). The dual-layer
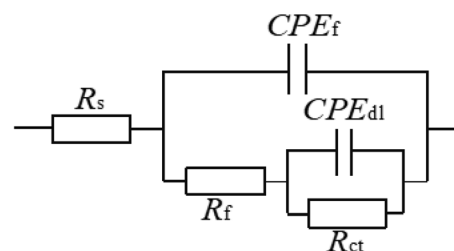

Fig. 9   Equivalent circuit diagram.

rust structure formed during corrosion introduces independent mass transport resistance (R_f) and capacitive response (CPE_f) of the corrosion product film, which cannot be fully characterized by simple three-element models accounting only for solution and double-layer effects. Meanwhile, EIS phase angle plots exhibit two distinct time constants, corresponding to the charge transfer at the substrate–electrolyte interface (R_{ct}/CPE_{dl}) and ion diffusion through the rust layer (R_f/CPE_f), providing direct experimental evidence for the multi-element model with film components. Additionally, the non-ideal capacitive behavior of the rust layer and electrical double layer (caused by surface roughness, inhomogeneous corrosion products, and adsorbed species) can be accurately described by constant phase element (CPE) instead of ideal capacitors to address the dispersion effect in impedance analysis.

The EIS parameters presented in Table 5 demonstrate distinct stages of corrosion evolution, as evidenced by variations in charge transfer resistance (R_{ct}) and corresponding statistical data. All fitting processes were performed using Zsimpwin software with a five-element equivalent circuit, and the reliability of fitting results was verified by chi-square (χ^2)

values. During the initial exposure period (2–4 days), a significant decrease in R_{ct} from 2860 to 1029 Ω cm^2, was observed, indicating accelerated reaction kinetics due to direct interaction between the bare steel surface and corrosive agents. This initial phase is characterized by minimal formation of protective rust layers, which corresponds with the observed rapid material degradation. Subsequent measurements revealed a notable increase in R_{ct} values, reaching 4263 Ω cm^2 by day 6 and peaking at 5421 Ω cm^2 on day 8. This upward trend correlates with the progressive development of compact corrosion products that effectively inhibit ionic transport. The maximum R_{ct} value recorded on day 8 confirms the optimal barrier properties achieved by the mature rust layers at this stage. However, a subsequent reduction in R_{ct} to 3815 Ω cm^2 by day 10 indicates structural degradation of the protective layer under prolonged exposure to Cl^-–HSO_3^- synergistic effects. This degradation is characterized by microcrack propagation and acidic dissolution processes, which increase the active surface area and consequently facilitate charge transfer processes. The observed trend reversal highlights the dynamic equilibrium between protective film growth and corrosive media penetration, where accumulated structural defects ultimately dominate the corrosion mechanism.[37] These quantitative impedance parameters are consistent with microscopic observations (Fig. 3 and 6) and elemental analysis results (Tables 2–4), collectively demonstrating the time-dependent competition between passivation and depassivation processes. The comprehensive data set provides valuable insights into the complex interplay of factors governing the corrosion behavior of the material under investigation.

Fig. 10 shows the polarization curves of A100 steel during corrosion in 5% NaCl solution. The anodic polarization curves
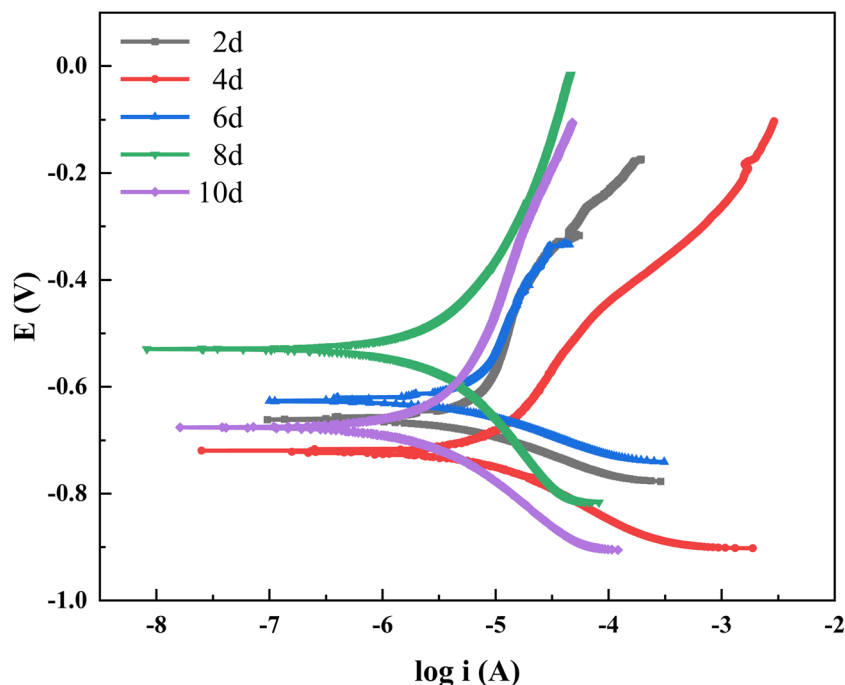
Table 6 Polarization curve fitting result

Salt spray time	E_{corr} (V)	I_{corr} (μA cm^{-2})	β_a (mV dec^{-1})	β_c (mV dec^{-1})
2 days	−0.663	5.093	128.6	112.3
4 days	−0.721	7.345	105.4	108.7
6 days	−0.625	4.064	146.2	115.8
8 days	−0.530	1.726	189.5	124.6
10 days	−0.672	23.442	89.7	96.4

Fig. 10 Polarization curve of A100 steel in 5% NaCl solution under different corrosion time.

exhibit similar characteristics, with the corrosion current increasing as the potential rises, indicating continuous dissolution and corrosion of the specimen. The fitting parameters of the polarization curves are presented in Table 6. The corrosion potential (E_{corr}) reflects the thermodynamic tendency of corrosion – a negative shift in E_{corr} corresponds to increased corrosion susceptibility, while a more positive E_{corr} indicate reduced corrosion activity. β_a reflects the kinetics of anodic Fe dissolution with smaller values indicating faster dissolution, while β_c relates to cathodic oxygen reduction and reflects changes in cathodic mechanism or mass transport resistance; at 2 days, moderate β_a (128.6 ± 8.5 mV dec^{-1}) and β_c (112.3 ± 7.9 mV dec^{-1}) indicate unobstructed reactions, 4 days sees β_a decrease to 105.4 ± 6.8 mV dec^{-1} (accelerated anodic dissolution) with stable β_c, 6 days shows increased β_a (146.2 ± 9.1 mV dec^{-1}) and β_c (115.8 ± 8.2 mV dec^{-1}) due to initial rust layer inhibition, 8 days achieves maximum β_a (189.5 ± 10.3 mV dec^{-1}) and β_c (124.6 ± 9.5 mV dec^{-1}) *via* dense dual-layer rust protection, and 10d witnesses β_a (89.7 ± 5.6 mV dec^{-1}) and β_c (96.4 ± 5.8 mV dec^{-1}) plummet as Cl$^-$–HSO$_3^-$ synergistic attack damages the rust layer, reactivating both anodic and cathodic reactions.

Table 6 presents the fitting parameters that illustrate the corrosion evolution of A100 steel. After a 2-days exposure, the corrosion potential (E_{corr}) is measured at −0.663 V, with a corrosion current density (I_{corr}) of 5.093 μA cm^{-2}. By day 4, E_{corr} shifts negatively to −0.721 V while I_{corr} increases to 7.345 μA cm^{-2}, indicating accelerated corrosion activity. On day 6, improved protection is observed as E_{corr} rises to −0.625 V and I_{corr} decreases to 4.064 μA cm^{-2}. Optimal performance is achieved on day 8, with a minimal I_{corr} of 1.726 μA cm^{-2} and maximum charge transfer resistance (R_{ct}), which corresponds to dense corrosion product layers that effectively isolate the substrate from the acidic electrolyte. However, by day 10, the degradation of protection results in a negative shift in E_{corr} to −0.672 V, with I_{corr} surging to 23.442 μA cm^{-2}. This acceleration is attributed to accumulated structural damage, an increased active surface area, and compromised rust layers under sustained HSO$_3^-$/Cl$^-$ attack, despite the slightly elevated E_{corr} suggesting a reduced thermodynamic tendency for corrosion.

3.3 Micro electrochemical testing results and analysis

Fig. 11 illustrates the surface potential distribution of A100 steel specimens exposed to salt spray and SO$_2$ corrosion over varying durations, as characterized by scanning Kelvin probe (SKP) measurements. The measured potential (E) profiles were

Table 7 Gaussian fitting result

Salt spray time per days	μ mV^{-1}	σ	Maximum potential (mV)	Minimum potential (mV)	Potential range (mV)
0	−159.46	62.83	227	−294	571
6	−62.01	85.96	95	−783	878
10	277.53	66.89	436	−282	718

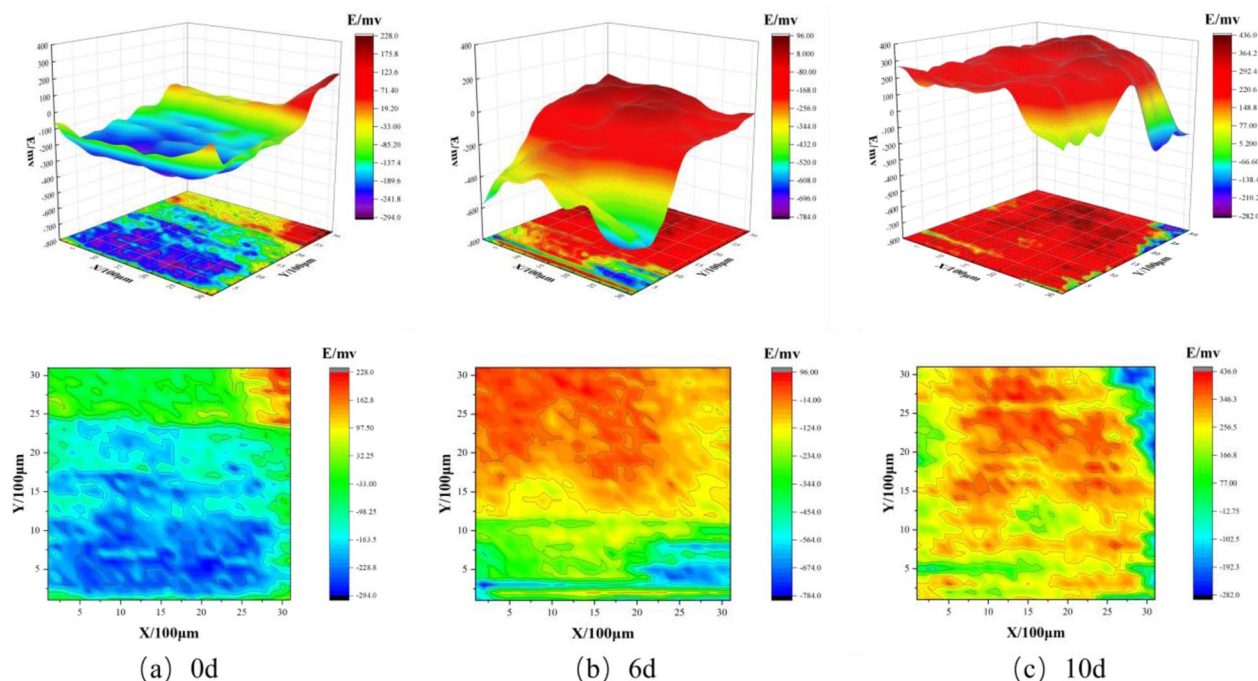**Fig. 11** Scanning Kelvin potential distribution after different time of salt spray-SO$_2$ test.

analyzed using Gaussian probability distribution fitting, represented by the following equation:

$$y = A \times \exp[-0.5(E - \mu)^2/\sigma^2] \tag{2}$$

where A denotes a normalization constant, μ represents the expectation value (mean potential), and σ quantifies the standard deviation (potential distribution dispersion). The fitting results, demonstrated in Fig. 12 and Table 7, reveal systematic evolution of surface electrochemical heterogeneity during corrosion progression.

Fig. 11 illustrates the evolution of surface potential characteristics during salt spray-SO$_2$ corrosion. The pristine specimen (0 days) exhibits a homogeneous potential distribution with minimal variation (mean: −159.46 mV, σ = 62.83), reflecting intrinsic micro-galvanic effects between alloying elements with differing electrochemical potentials.[38,39] After 6-days exposure, the potential distribution broadens significantly (−783 mV to 95 mV), accompanied by an increased standard deviation (σ = 85.96) and anodic shift (mean: −62.01 mV), indicative of intensified localized corrosion. This transformation results from chloride-induced breakdown of passive films and subsequent micro-galvanic coupling between active substrate regions (anodes) and secondary phase particles/corrosion products (cathodes).[40,41] The expanded potential range correlates with accelerated corrosion kinetics due to the cathodic activation of inclusions and microstructural heterogeneities.[42,43] By day 10, the surface potential further elevates (mean: 277.53 mV, σ = 66.89) with reduced potential fluctuation, contrasting with electrochemical test trends but aligning with microscopic observations of complete rust coverage. This apparent discrepancy stems from SKP's sensitivity to surface oxide properties, in contrast to electrochemical measurements that reflect bulk charge transfer processes influenced by HSO$_3^-$/Cl$^-$ penetration and multi-layer corrosion products. It is clarified that the Kelvin potential measured by SKP reflects the surface work function rather than direct corrosion rate, which is dominated by charge transfer kinetics (characterized by EIS and polarization parameters). This explains the discrepancy between SKP and electrochemical trends: SKP is sensitive to surface rust layer integrity, while EIS/polarization tests reflect bulk corrosion involving HSO$_3^-$/Cl$^-$ penetration. For example, the elevated Kelvin potential at 10d corresponds to sulfur-containing rust (confirmed by XPS/EDS) but does not indicate reduced corrosion activity—consistent with the surged Icorr and dropped R_{ct} in electrochemical tests. The progressive Kelvin potential with exposure duration consistently corresponds with EIS evolution and morphological changes, demonstrating complementary insights from surface-sensitive and bulk electrochemical characterization techniques.

3.4 EBSD results and analysis

Fig. 13 displays inverse pole figures of A100 steel substrate specimens obtained through orientation imaging microscopy at various corrosion durations. The uncorroded specimen presents distinctly visible grain structures. With increasing corrosion time, corrosion products accumulate on the surface, and the grain size distribution shows subtle changes.[44,45] Statistical analysis of grain orientations indicates a gradual reduction in low-angle grain boundaries as corrosion advances (Fig. 13b). The grain orientation distribution becomes increasingly heterogeneous, indicating the selective dissolution of specific crystallographic orientations (particularly the (111) orientation marked in Fig. 13a) and structural adjustments related to corrosion-induced phase interactions.[44,45]

Fig. 14 presents phase diagrams and pole figures of A100 steel after 2, 4, 6, and 10 days of corrosion, with austenite (green) and martensite (red) phases clearly identified. The fraction of the austenite phase initially decreases and then increases during corrosion (Fig. 14a), a phenomenon attributed to the formation of passive films on the surfaces of austenite. Austenite's higher chemical activity and lower corrosion resistance render it more susceptible to attack than martensite,

Table 8 Phase fraction data

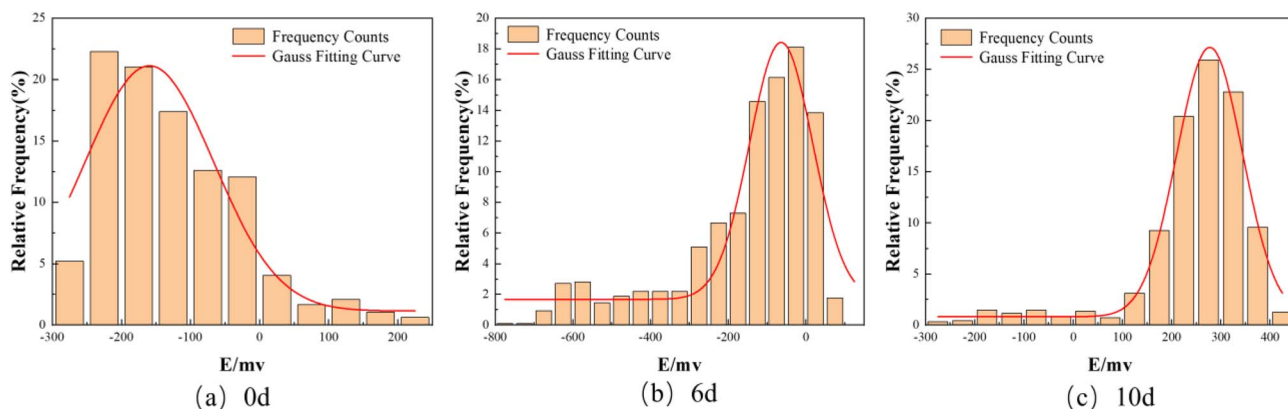|	2 days	4 days	6 days	10 days
Fe(Alpha, Martensite, BCC)	0.985	0.992	0.991	0.861
Fe(Gamma, Austenite, FCC)	0.015	0.008	0.009	0.139

Fig. 12 Guassian probability distribution of surface potential of A100 steel at different times.

leading to reduced austenite volume fraction in early stages (Table 8). By day 6, accumulated corrosion products form protective passive films on austenite, inhibiting further corrosion,[46] while partial dissolution of martensite leads to a decrease in its phase fraction. However, due to the protective effect of the austenite passive film, the austenite volume fraction increased, resulting in a significant elevation of the

austenite phase proportion after 10 days of corrosion. The pole figures (Fig. 14b and c) demonstrate weakened characteristic peaks for both phases with prolonged exposure, indicating structural degradation. Initial-stage austenite retains partial orientation features, likely due to preserved passive films, the emergence of new orientation peaks suggest possible recrystallization. Corroded martensite exhibits randomized
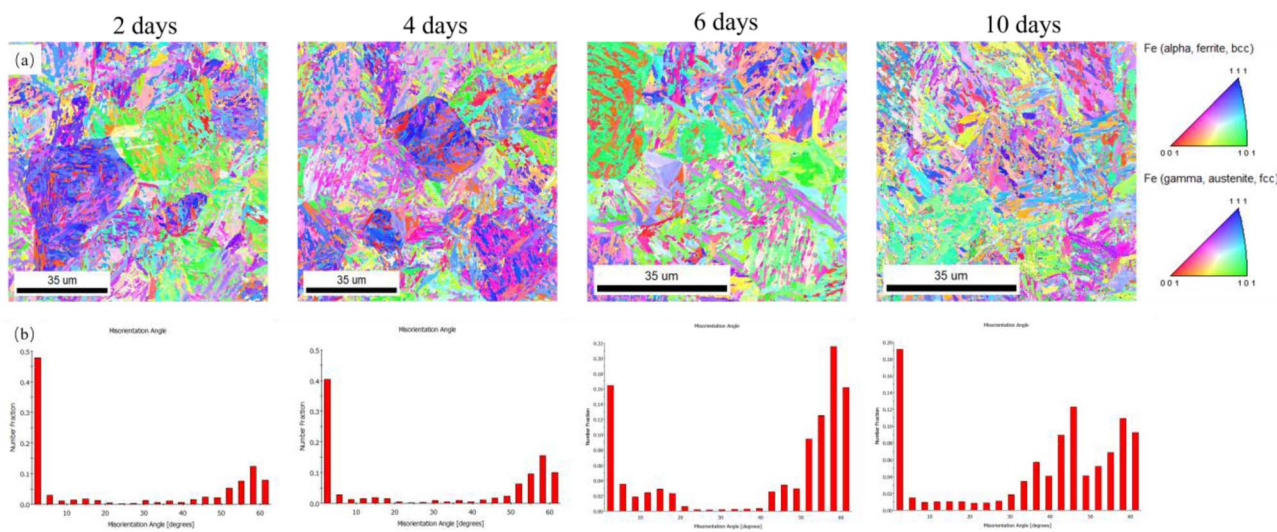

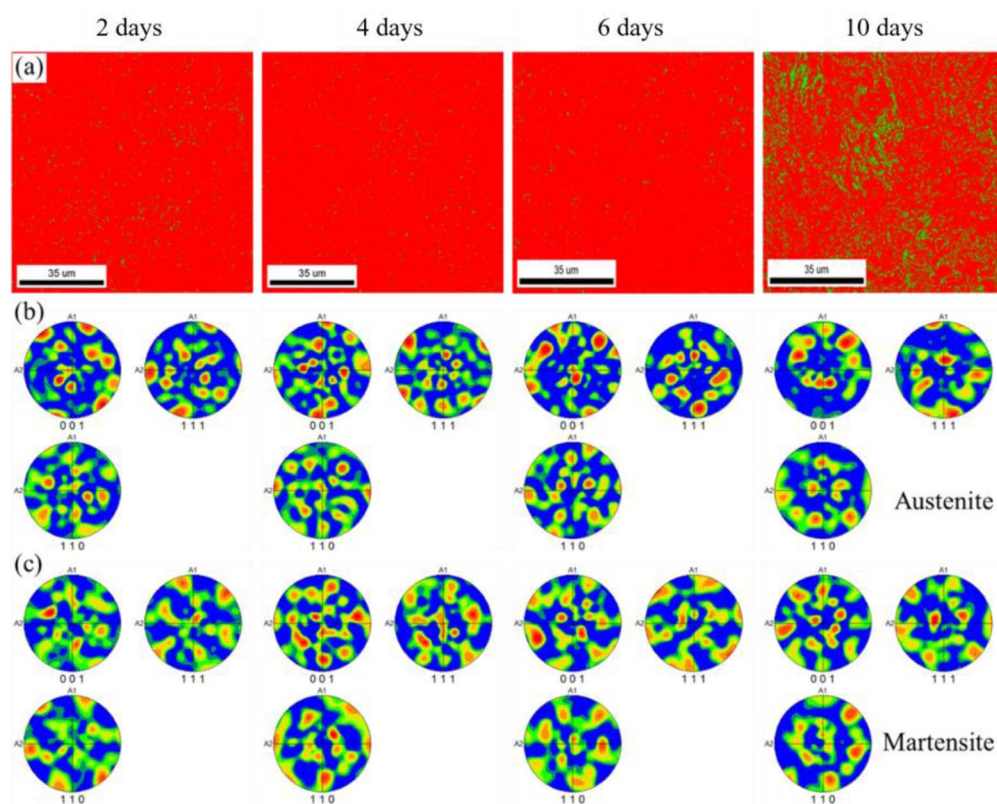Fig. 13 (a) Reverse polarity diagram of A100 steel sample (b) grain orientation statistics.

Fig. 14 (a) Phase diagram of A100 steel sample (b and c) austenite and ,artensite pole diagrams of A100 steel sample.

rate.

orientations, reflecting its propensity for brittle fracture propensity during corrosion. These phase-specific evolution patterns reveal that although austenite is initially vulnerable, early passivation temporarily retards corrosion. However, the subsequent dynamic equilibrium between phase dissolution and re-exposure ultimately accelerates degradation by day 10, consistent with electrochemical analyses that indicate a renewed escalation in the corrosion rate.

Fig. 15a displays grain boundary maps of A100 steel at different corrosion stages, with red, green, and blue lines representing boundaries having misorientation angles below 5°, between 5°–15°, and above 15°, respectively. Progressive corrosion induces significant increases in both grain boundary density and the proportion of high-angle boundaries (Table 9). This phenomenon arises from two concurrent mechanisms: (1) corrosion-induced grain dissolution promotes grain refinement and structural rearrangement, as corroborated by grain size

evolution statistics in Fig. 15b; (2) preferential corrosion attack along original grain boundaries transforms initially planar boundaries into irregular configurations, leading to increased high-angle boundary formation.

3.5 Analysis of corrosion behavior mechanism

During salt spray-SO_2 testing, a depolarization reaction occurs at the cathode through oxygen participation, constituting a critical step in the corrosion process and typically manifested as localized oxidation features. The anodic reaction predominantly proceeds at the steel substrate/rust layer interface, while cathodic reactions dominate in the outer regions of the inner rust layer. Electrochemical analysis coupled with surface morphological observations reveals that corrosive media penetration to the substrate surface induces localized attack, ultimately forming characteristic corrosion pits.

The synergistic effect of Cl^- and HSO_3^- is not a simple superposition of individual effects but a mutual promotion mechanism: Cl^- preferentially adsorbs on the passive film surface, displacing oxygen atoms to form unstable Fe–Cl complexes that break the film and create corrosion channels, while HSO_3^- derived from SO_2 dissolution acidifies the local environment (pH $\approx$ 4.2–4.8) to accelerate anodic dissolution of Fe and react with Fe_3O_4 in the inner rust layer to generate porous $FeSO_4$. These channels facilitate HSO_3^- penetration to

Table 9 Grain boundary-legend

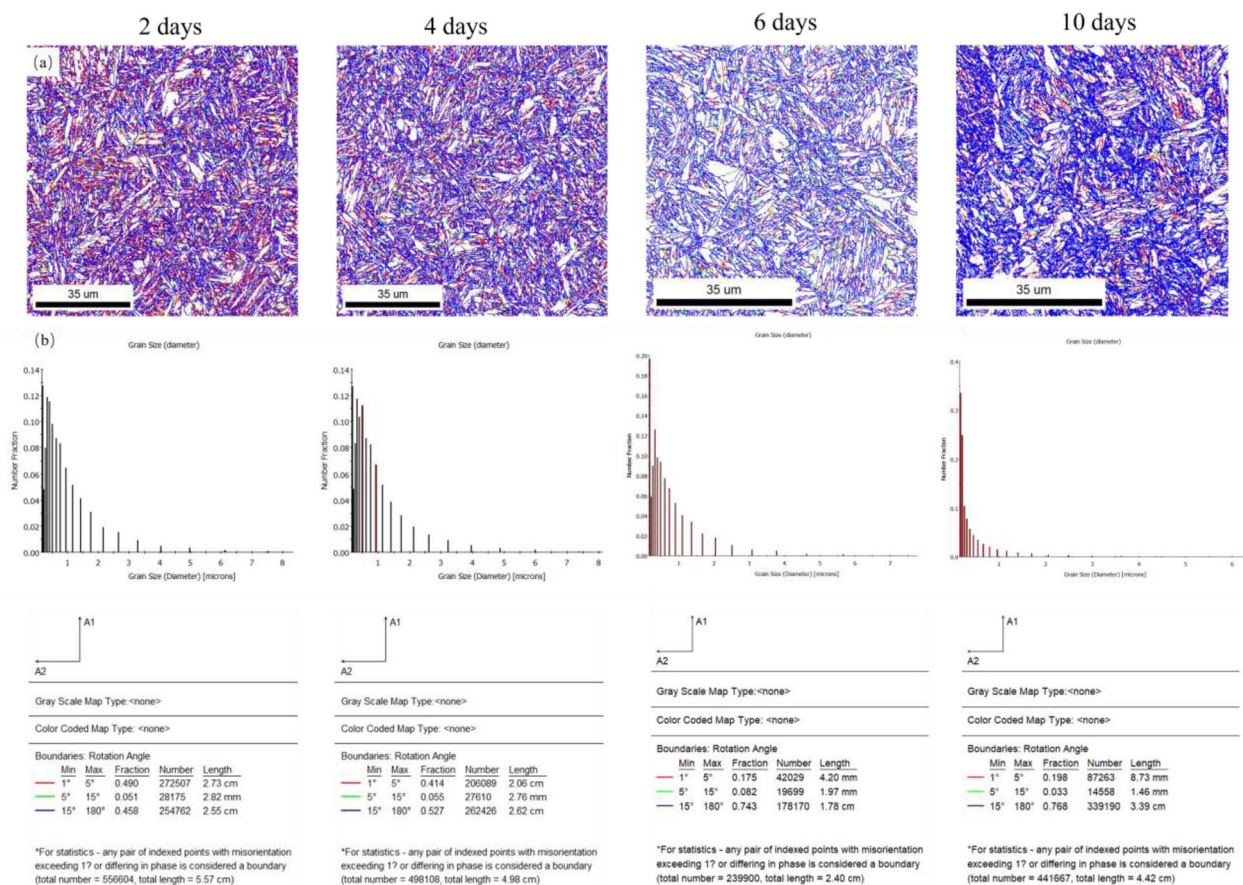|	2 days	4 days	6 days	10 days
LAGB	0.541	0.469	0.257	0.231
HAGB	0.458	0.527	0.743	0.768
Percentages of LAGB/HAGB	1.181	0.889	0.346	0.301

Fig. 15 (a) Grain boundary diagram of A100 steel sample (b) corresponding to grain size of samples with different corrosion times.
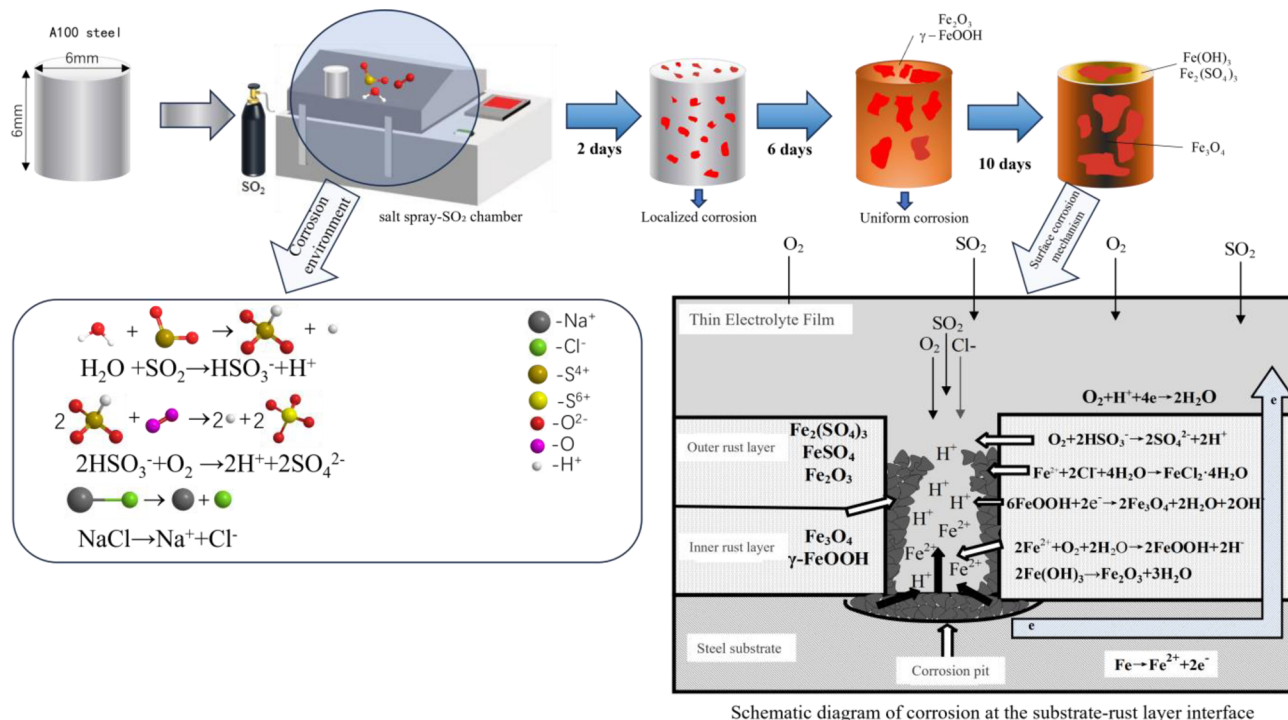
Fig. 16 Analysis of corrosion behavior mechanism.

the substrate, and the acidic environment further enhances Cl^- solubility and mobility, forming a positive feedback loop that rapidly degrades the rust layer. This synergy is verified by EDS/XPS results (Tables 2–4 and Fig. 5) showing coexistence of S and Cl^- in corrosion regions, and electrochemical data where the Icorr at 10d (23.442 μA cm^{-2}) is much higher than the sum of corrosion rates induced by single Cl^- or SO_2 environments.

Fig. 16 illustrates the corrosion mechanism of A100 steel. During the initiation stage, active iron in the substrate acts as an anode, generating Fe^{2+} through electron loss. This Fe^{2+} reacts with dissolved oxygen to form FeOOH deposits at pit bases. Concurrently, chloride ions participate in complex reactions with Fe^{2+}, producing corrosive $FeCl_2 \cdot 4H_2O$ that accelerates surface degradation. Sulfur dioxide-derived HSO_3^- further oxidizes to SO_4^{2-}, forming iron sulfates ($Fe_2(SO_4)_3$/$FeSO_4$) within corrosion products. $Fe(OH)_2$ decomposition yields FeO, which reacts with oxygen to generate FeOOH, while $Fe(OH)_3$ transforms into stable Fe_2O_3 and Fe_3O_4. These oxides gradually develop a dense protective layer that impedes oxygen/chloride diffusion, creating oxygen concentration cells through restricted transport channels and increasing interfacial impedance. The combined effects of protective oxide formation and reduced anodic active area collectively decelerate corrosion rates during later initiation stages through modified electrochemical reaction kinetics.

4 Conclusion

This study investigates the early-stage corrosion behavior of A100 steel under salt spray-SO_2 conditions through comprehensive characterization and electrochemical analysis, yielding three principal conclusions:

(1) The corrosion process transitions from localized to generalized attack. The inner rust layers primarily consist of dense black Fe_3O_4 and γ-FeOOH, while outer layers consist of porous reddish-brown Fe_2O_3. After 10 days of exposure, yellowish outer rust forms, with XPS and FT-IR confirming the incorporation of sulfate and the predominance of Fe^{3+}.

(2) The corrosion follows triphasic kinetics: initial rapid corrosion (0–4 days) with charge transfer resistance (R_{ct}) decreasing from 2860 Ω cm^2 to 1029 Ω cm^2 and corrosion current density (I_{corr}) increasing from 5.09 μA cm^{-2} to 7.35 μA cm^{-2}; decelerated degradation (4–8 days) due to protective rust layer formation, with R_{ct} peaking at 5421 Ω cm^2 and I_{corr} dropping to the minimum of 1.73 μA cm^{-2}; renewed acceleration (8–10 days) induced by Cl^--HSO_3^- synergy, with R_{ct} plummeting to 426 Ω cm^2 and Icorr surging to 23.44 μA cm^{-2}.

(3) Macroscopically, the accumulation of corrosion product (Fe_3O_4/γ-FeOOH) temporarily inhibits corrosion until structural degradation from Cl^-–HSO_3^- penetration and autocatalytic occluded cell effects reignites propagation. Microstructurally, the initial passivation of austenite delays corrosion, the subsequent dissolution of martensite and the establishment of a dynamic phase equilibrium ultimately expose austenite, accelerating degradation beyond day 10. These findings systematically elucidate the interplay between corrosion product evolution, electrochemical dynamics, and microstructural modifications that govern the degradation mechanisms of A100 steel.

(4) The limitation of this study lies in the simulation of only the synergistic effect between sulfur dioxide (SO_2) and chloride

ions (Cl^-), without considering other pollutants commonly present on ship decks, such as nitrogen oxides (NO_x). Future work could focus on expanding the range of pollutants to better replicate real-world environmental conditions, extending the testing duration to investigate long-term corrosion evolution, and incorporating operational loads on landing gear structures to study stress–corrosion coupling behavior.

Conflicts of interest

There are no conflicts to declare.

Data availability

The data that support the findings of this study are included in the main text of the article. The detailed original experimental data, including scanning electron microscopy (SEM) micrographs, X-ray diffraction (XRD) patterns, X-ray photoelectron spectroscopy (XPS) data, Fourier transform infrared spectroscopy (FT-IR) data, energy dispersive spectroscopy (EDS) elemental mapping results, electron backscatter diffraction (EBSD) orientation data, and original datasets of electrochemical tests (electrochemical impedance spectroscopy (EIS), polarization curves, micro-area electrochemical tests, and scanning Kelvin probe (SKP)), are authentic and valid.

Should the original data or additional material data be required to replicate this study or validate the research results, they can be obtained from the corresponding author upon reasonable request.

Acknowledgements

References

1 Y. L. Chen, Z. Z. Zhang, N. K. Yao, et al., Initial Corrosion Behavior of Non-nitriding and Nitriding 38CrMoAl Steel in Salt Spray Environment, Surf. Technol., 2021, 50(01), 383–394.

2 A. Qian, P. Jin, X. M. Tan, et al., Corrosion and Electrochemical Properties of AerMet100 Steel in Salt Fog, Surf. Technol., 2018, 47(10), 231–239.

3 Z. R. Xian, L. Dong, L. An, et al., Microstructure characterization and mechanical behavior of laser additive manufactured ultrahigh-strength AerMet100 steel, Mater. Sci. Eng., A, 2016, 663, 69–77.

4 B. H. Ya, F. D. Chao, L. Hong, et al., Study on the Hydrogen Embrittlement of Aermet100 Using Hydrogen Permeation and SSRT Techniques, Metall. Mater. Trans., 2017, 48, 4046–4057.

5 J. K. Guo, J. S. Yu, X. Peng, et al., Study on the Atmospheric Corrosion Behavior of Carbon Steel Using Accelerated Corrosion Test, Surf. Technol., 2014, 43(04), 68–73.

6 Z. G. Zhang, J. Y. Zhai and Y. K. Gao, Application Research of Shot Peening Process on 300M Steel Surface, Surf. Technol., 2016, 45(04), 65–68.

7 T. Huang, X. P. Chen, X. D. Wang, et al., A Study on the Rust Characteristics and Corrosion Resistance of High Strength Weathering Steels in NaCl Solution, J. Mech. Eng., 2017, 53(20), 45–53.

8 Q. Xiang, X. P. Jiang, D. Zhao, et al., Effect of carbonitride treatment temperature on microstructure and corrosion resistance of TA2 titanium alloy, J. Xuzhou Normal Univ., 2021, 39(05), 87–91.

9 M. X. Guo, C. Pan, Z. Y. Wang, et al., A Study on the Initial Corrosion Behavior of Carbon Steel Exposed to a Simulated Coastal-Industrial Atmosphere, Acta Metall. Sin., 2018, 54(01), 65–75.

10 X. X. Song, Research on the Initial Corrosion Behavior of Carbon Steel in Typical Environments of Nuclear Power Plants, University of Science and Technology of China, 2020.

11 A. Qian, X. H. Yang, P. Jin, et al., Micro-zone Electrochemical Behavior of AerMet100 Steel in Salt Spray Environment under Cl^-, Equip. Environ. Eng., 2019, 16(10), 88–94.

12 A. Qian, P. Jin, X. M. Tan, et al., Effect of Shot Peening on Surface Integrity and Fatigue Properties of AerMet100 Steel, Surf. Technol., 2019, 48(09), 158–166.

13 W. D. Yang, L. H. Zhao, M. L. Shen, et al., Study on corrosion behavior of $CoCrNiNb_{0.1}+B_4C$ high entropy alloy coating on A100 ultra-high strength steel by laser cladding under simulated Marine environment, Surf. Technol., 2024, 1–13.

14 Bachhar, V. Joshi, R. Haldhar, et al., A sustainable triple-action inhibitor: Corrosion protection, antioxidant activity, and antibacterial performance of Solanum chrysotrichum fruit extract, Bioresour. Technol., 2025, 133385.

15 Joshi, V. Bachhar, P. Singh, et al., Rheological and anticorrosion study of Piper chaba extract and coating for mild steel in 2M H2SO4, Colloids Surf., A, 2024, 708, 135989.

16 L. Xu, Y. L. Chen, S. G. Wu, et al., The Study about the Deck Park Environment of Carrier-Based Aircraft and Corrosive State, Aircraft Des., 2016, 36(06), 54–57.

17 S. J. Ketcham, Accelerated Laboratory Corrosion Test for Materials and Finishes Used in Naval Aircraft, Naval Air Development Center, Report No NADC-77252- 3, 1977, 1977.

18 J. Y. Zhu, M. Li and C. G. Cheng, Development and Enlightenment of "Salt Spray-SO2" Test Method for Carrier-based Aircraft of US Navy, Equip. Environ. Eng., 2017, 14(03), 1–6.

19 K. Dhakane, The green fix: environmentally friendly corrosion protection for mass produced metal fasteners, Surf. Coating. Int., 2011, (2), 94.

20 B. D. Sartwell, K. O. Legg, J. Zimmerman, M. Reynolds, J. Gribble, J. Magno and R. Mason, Validation of HVOF Thermal Spray Coatings as a Replacement for Hard Chrome Plating on Hydraulic/Pneumatic Actuators, ESTCP Cost and Performance Report, U.S. Department of Defense, Arlington, VA, 2004.

21 A. Schwartz and E. Beck, Corrosion Performance of AlumiPlate Coated Electrical Connectors with Trivalent Cr Post-Treatment, Naval Air Systems Command, 2007.

22 X. J. Wu, Y. L. Chen, G. X. Bian, *et al.*, Initial Corrosion Behavior of Non-nitriding and Nitriding 38CrMoAl Steel in Salt Spray Environment, *Surf. Technol.*, 2022, **51**(05), 234–244.

23 Z. L. Wei, G. X. Bian and A. D. Wang, Effect of Surface Shot Peening on Corrosion Resistance of Aermet100 Steel, *Equip. Environ. Eng.*, 2023, **20**(02), 73–81.

24 W. Zhou, W. Lan, S. Zhao, *et al.*, Corrosion Behavior of 42CrMo Steel in Chloride Solution, *Surf. Technol.*, 2017, **46**(08), 216–220.

25 C. C. Zhou, C. Li, J. Y. Qian, *et al.*, Adsorption performance of iron oxide red on antimony (V) in printing and dyeing wastewater, *J. Zhejiang Univ. (Sci. Ed.)*, 2022, **49**(02), 201–209.

26 D. H. Wang, Z. H. Zhang, P. Li, *et al.*, XPS Study on Hydrogen Sulfide Corrosion Products from Ferric Oxide, *Corrosion Sci. Protect. Technol.*, 2017, **03**, 008.

27 Y. Ma, L. Ying and F. Wang, Corrosion of low carbon steel in atmospheric environments of different chloride content, *Corros. Sci.*, 2009, **51**, 997–1006.

28 Y. L. Chen, A. D. Wang, Y. Zhang, *et al.*, The Synergistic Effect of Cl^- and H^+ on Initial Corrosion of 2024-T3 Aluminum Alloy, *Mater. Rep.*, 2018, **32**(09), 1549–1556.

29 W. Zhou, W. Lan, S. Zhao, *et al.*, Corrosion Behavior of 42CrMo Steel in Chloride Solution, *Surf. Technol.*, 2017, **46**(08), 216–220.

30 J. H. Yang, Q. Y. Liu, X. D. Wang, *et al.*, The Progress of Investigation on Weathering Steel and Its Rust Layer, *J. Chin. Soc. Corrosion Protect*, 2007, (06), 367–372.

31 Y. Xia, F. H. Cao, L. R. Chang, *et al.*, Corrosion Micro-and Macro-electrochemical Behavior of Rusted Carbon Steel and Weathering Steel, *Chem. J. Chin. Univ.*, 2013, **34**(05), 1246–1253.

32 X. G. Zheng, W. D. fu, H. Peng, *et al.*, Preparation and characterization of Cu x Zn 1-x S nanodisks for the efficient visible light photocatalytic activity, *J. Environ. Chem. Eng.*, 2017, **6**, 9–18.

33 L. L. Wu, *Generation of Persulfate in Electrolytic System and Treatment of Oilfield Wastewater*, Dalian Maritime University, 2023.

34 C. Wei, L. Z. Huai, Z. Jun, *et al.*, Study on the Preparation of A New Composite Coagulant: Poly-Ferric-Titanium-Sulfate and Analysis of FTIR Spectrum and UV-Vis Spectrum, *Spectrosc. Spectral Anal.*, 2016, **36**(04), 1038–1043.

35 H. Sheng, C. F. Dong, K. Xiao, *et al.*, Effect of pH on Electrochemical Behavior of 2024-T351 Aluminium Alloy in NaCl Solution, *Corrosion Protect*, 2013, **34**(02), 107–110.

36 D. M. I. Kharitonov, Corrosion Inhibition of Aluminum Alloy AA6063-T5 by Vanadates: Microstructure Characterization and Corrosion Analysis, *J. Electrochem. Soc.*, 2018, **165**, C116–C126.

37 Y. L. Chen, Z. Z. Zhang, Y. Zhang, *et al.*, Effect of Salt Spray Corrosion Environment on Dynamic Mechanical Properties of 38CrMoAl Steel, *Rare Met. Mater. Eng.*, 2021, **50**(06), 2040–2051.

38 Y. L. Chen, H. L. Huang, Y. Zhang, *et al.*, Study on Equivalent Conversion of Galvanic Corrosion Under Different Liquid Film Thickness, *Mater. Rep.*, 2018, **32**(09), 1571–1576.

39 G. X. Bian, Y. L. Cheng, Y. Zhang, *et al.*, Equivalent Conversion Coefficient of Aluminum/Titanium Alloy Between Acidic NaCl Solution with Different Concentration and Water Based on Galvanic Corrosion Simulation, *Mater. Rep.*, 2019, **33**(16), 2746–2752.

40 B. Losiewicz, M. Popczyk, M. Szklarska, *et al.*, Application of the Scanning Kelvin Probe Technique for Characterization of Corrosion Interfaces, *Solid State Phenom.*, 2015, **228**, 369–382.

41 N. E. Benaioun, I. Maafa, A. Florentin, *et al.*, Time dependence of the natural passivation process on AISI 304 in an alkaline medium: Atomic force microscopy and scanning Kelvin probe force microscopy as additional tools to electrochemical impedance spectroscopy, *Appl. Surf. Sci.*, 2018, **436**, 646–652.

42 M. Iannuzzi, K. L. Vasanth and G. S. Frankel, Unusual Correlation between SKPFM and Corrosion of Nickel Aluminum Bronzes, *J. Electrochem. Soc.*, 2017, **164**, C488–C497.

43 A. Nazarov, F. Vucko and D. Thierry, Scanning Kelvin Probe for detection of the hydrogen induced by atmospheric corrosion of ultra-high strength steel, *Electrochim. Acta*, 2016, **216**, 130–139.

44 Y. Ma, X. Zhou, Y. Liao, Y. Yi, H. Wu, Z. Wang and W. Huang, Localised corrosion in AA 2099-T83 aluminium-lithium alloy: The role of grain orientation, *Corros. Sci.*, 2016, **107**, 41–48.

45 Q. Zhou, Z. Zheng and Y. Gao, Abnormal selective dissolution by the partial recrystallization in a plastically deformed austenitic stainless steel, *Corros. Sci.*, 2021, **188**, 109548.

46 G. Tranchida, M. Clesi, F. Di Franco, F. Di Quarto and M. Santamaria, Electronic properties and corrosion resistance of passive films on austenitic and duplex stainless steels, *Electrochim. Acta*, 2018, **273**, 412–423.